



Effect of particulate/matrix debonding on the formation of adiabatic shear bands

B.M. Love^a, R.C. Batra^{b,*}

^a U.S. Army Research Laboratory, Impact Physics Branch, Aberdeen Proving Grounds, MD 21005-5069, USA

^b Virginia Polytechnic Institute and State University, Department of Engineering Science and Mechanics, Blacksburg, VA 24061, USA

ARTICLE INFO

Article history:

Received 28 July 2009

Received in revised form

19 October 2009

Accepted 27 October 2009

Available online 3 November 2009

Keywords:

Debonding

Adiabatic shear bands

Cohesive zone failure criterion

Finite element method

ABSTRACT

We use the cohesive zone failure model to simulate debonding and failure in high strain-rate plane strain deformations of a heat conducting particulate composite comprised of initially circular metallic particulates immersed in a metallic matrix, with the goal of delineating the effect of these failures on the initiation and propagation of adiabatic shear bands (ASBs). Failure is assumed to ensue at an interface between two elements when a predefined combination of the normal and the tangential tractions on that interface reaches a critical value. We postulate that the critical value of the traction in the cohesive zone failure model decreases affinely with an increase in the temperature. Both particulate and matrix materials are assumed to be isotropic, heat conducting, and to obey the von Mises yield criterion with the flow stress depending upon the effective strain, the effective strain rate, and the temperature according to the Johnson–Cook relation. The coupled transient thermomechanical problem is analyzed by the finite element method by using 3-node triangular elements and the finite calculus technique to prevent volumetric locking. It is found that the critical strength of the bond between the particulate and the matrix significantly influences the loss of strength of the entire specimen. The time of initiation of an ASB is influenced by the time when debonding ensues which depends upon the values of the critical traction and the mode-mixity parameter in the cohesive zone failure criterion.

© 2009 Elsevier Ltd. All rights reserved.

1. Introduction

As modeling and simulation is increasingly used to predict the behavior of structures and systems under catastrophic loading, simulation techniques and physical models for dynamic failure have become very important. Dynamic failure of ductile materials is quite often preceded by the initiation and development of adiabatic shear bands (ASBs) which are narrow regions, a few micrometers wide, of intense plastic deformation. ASBs are known to play a significant role in penetration problems, and machining and metal-forming processes. For example, Magness and Farrand [1] have postulated that if in a penetration problem ASBs continuously form and lead to failure near the nose of the projectile, resulting in a projectile with a sharp, rather than a mushroomed, nose, then the penetration depth will be more than that for the case of no ASB formation. Similarly, ASBs facilitate the punching of a hole in a metal cutting process since the kinetic energy required for punching a centimeter thick plate

by plugging equals nearly that needed to indent the same plate by less than 1 mm.

Tresca [2] observed ASBs (he called them hot lines) over a century ago during the hot forging of a platinum bar. Subsequently they were reported by Massey [3]. However, Zener and Hollomon's [4] observing them during the punching of a hole in a low carbon steel plate, and proposing that they form when softening of the material due to its being heated up has overcome its hardening due to strain- and strain-rate effects generated considerable interest in the field. Clifton [5] used the criterion that an ASB initiates when the shear stress in quasi-static simple shearing deformations of a homogeneous body attains its maximum value to find the shear strain at the initiation of an ASB in a thermoviscoplastic material obeying a power-law type relation among the shear stress, the shear strain and the temperature rise. Bai [6] postulated that an ASB initiates when infinitesimal perturbations superimposed on finite homogeneous deformations of a body begin to grow. Wright and Walter [7] built upon the numerical solution of Wright and Batra [8] to show that the shear stress collapses at the initiation of an ASB. These results were confirmed experimentally by Marchand and Duffy [9] during torsional deformations of thin-walled tubes. They also reported the shear strain within an ASB being as large as 20. Even though heat conduction plays a significant role in determining the ASB

* Corresponding author.

E-mail addresses: bryan.m.love@arl.army.mil (B.M. Love), rbatra@vt.edu (R.C. Batra).

width, the band is called adiabatic since there is not enough time for the heat to be conducted away from it. Numerical solutions of the coupled nonlinear equations governing simple shearing and plane strain thermomechanical deformations of a thermoelasto-viscoplastic body reveal that an ASB forms much later than when the effective stress attains its maximum value (e.g. see Batra [10]), and the delay between these two instants depends upon the number, the size and the type of defects present in the body. Much of the earlier work on ASBs is summarized in Bai and Dodd's [11] book, the book edited by Perzyna [12], and the review paper by Tomita [13]. Mathematical aspects of the ASB phenomenon are described in Wright's [14] book.

Works enumerated above and numerous others have studied the shear banding phenomenon in homogenous materials. However, many materials are inhomogeneous because of impurities and/or second-phase particles, which are frequently introduced in order to strengthen the material (or give some other desirable property). One such class of materials is metal-particulate/metal-matrix composites, which are frequently produced to tailor bulk properties (density, failure strength, ductility) by varying the volume fraction of two dissimilar constituents.

ASBs in particulate composites have been studied both experimentally (e.g. see Zhou et al. [15]) and numerically (e.g. see Zhou [16], Batra and Wilson [17], Batra and Love [18]). The latter approach has considered both homogenized materials (e.g. see Batra and Love [19]) and analyzing deformations of each constituent (Zhou [16], Batra and Love [18]). During their analyses of a particulate composite by the finite element method (FEM) Batra and Love [18] found that the ASB initiation criterion for a homogeneous material does not apply to particulate composites, and proposed the following alternative criterion: an ASB initiates at a point when the energy dissipation rate there suddenly increases by nearly an order of magnitude. This ASB initiation criterion has subsequently been adopted by Charalambakis and Baxevanis [20] and Batra and Love [19]. Zhu and Batra [21] analyzed the initiation and propagation of ASBs in plane strain deformations of laminated composites, and found that an ASB initiating from a point on an interface between two adjoining layers propagated easily into the softer material. Batra and Kwon [22] studied ASB initiation in simple shearing deformations of a bimetallic body with a defect placed at the interface between the two materials and found that the ratio of the shear moduli of the two materials significantly influenced which material shear banded.

It has been conjectured that during high strain rate deformations of particulate composites, particulates debond from the matrix resulting in the loss of load transfer between the two constituents, preventing or significantly delaying the initiation and development of ASBs. Depending upon the strength of the particulate and the matrix materials and the bond between them, failure may initiate in either constituent or along particulate/matrix interfaces. This differs from earlier studies on ASBs in delineating how crack formation and particulate/matrix debonding affect the formation and evolution of ASBs. This additional knowledge in failure mechanics would allow particulate composites to be constructed such that the ASB formation could be deliberately reduced or enhanced.

In order to make the problem tractable with reasonable computational resources, we adopt a cohesive-zone technique to simulate failure at a point. That is, the formation of a crack is determined by a small dissipative region called a cohesive zone, where the combination of tractions and opening displacements determine the level of failure of a material or of an interface between two distinct materials. The cohesive zone method allows numerical simulation of failure at multiple locations in the body simultaneously and allows these failures to interact.

Dugdale [23] and Barenblatt [24] proposed the use of cohesive zones to model material failure and generate traction-free crack surfaces. Xu and Needleman [25] and Camacho and Ortiz [26] introduced this theory in the FE methodologies to simulate fracture along inter-element boundaries. The technique has been used by numerous researchers to study material failure and delamination of composites. Computed results depend upon values assigned to material parameters in the cohesive zone relation, and to some extent on the FE mesh. In this work cohesive zones are inserted adaptively when surface tractions at an interface between two adjoining FEs reach a critical value. A limitation of this approach is that failure is only allowed to ensue along element boundaries and, therefore, computed results are mesh dependent. Using randomly oriented FEs and conducting the same analysis with multiple meshes is required to increase confidence in results.

The rest of the paper is organized as follows. The problem studied is formulated in Section 2 that also describes the cohesive zone relation and the ASB initiation criterion. The computational algorithm is briefly discussed in Section 3. Results including the effect of the particulate/matrix interfacial strength on the development of ASBs are discussed in Section 4. In Section 5 we remark on similarities and differences between the cohesive zone and the nodal release techniques. Conclusions of this work are summarized in Section 6.

2. Formulation of the problem

2.1. Governing equations

A schematic sketch of the problem studied is shown in Fig. 1. Because of the assumption of plane strain deformations the dimension of the prismatic body perpendicular to the cross section shown in Fig. 1 is very large. A 2 mm × 2 mm square particulate composite body is compressed by applying in the vertical direction an axial velocity $V(t) = 20 \text{ m/s} = 0.02 \text{ mm}/\mu\text{s}$ on the top surface while the bottom surface rests on a rigid and frictionless surface. The prescribed velocity increases linearly from zero to its steady state value in 1 μs , giving the steady state nominal axial strain-rate of 10,000/s. Circular cylindrical

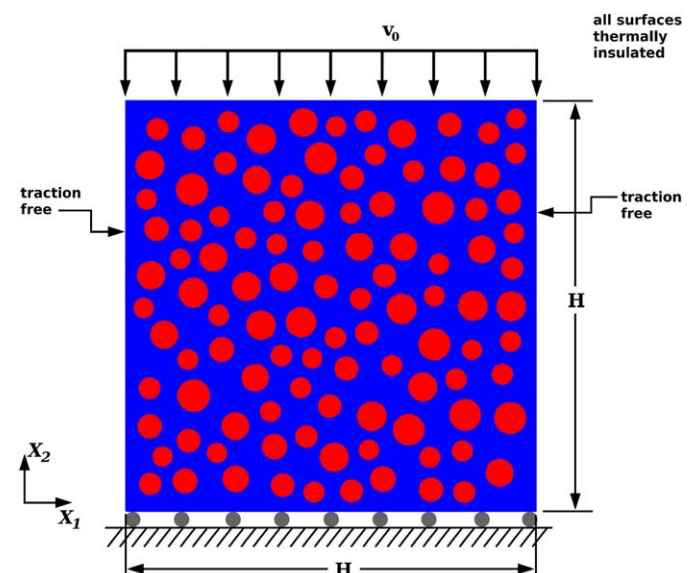


Fig. 1. Schematic sketch of the problem studied.

particulates of diameters ranging from 50 to 80 μm are randomly placed in a metallic matrix.

We use the referential description of motion and rectangular Cartesian coordinates to describe the dynamic thermo-mechanical deformations of the particulate composite. Both the particulate and the matrix materials are modeled as heat-conducting, isotropic, homogeneous thermo-elasto-viscoplastic and exhibit strain and strain-rate hardening and thermal softening. These are characterized by the Johnson–Cook [27] empirical viscoplastic relation:

$$\sigma_y = (A + B(\epsilon_e^p)^n) \left(1 + C \ln \left(\frac{\dot{\epsilon}_e^p}{\dot{\epsilon}_0} \right) \right) (1 - T^m) \quad (1)$$

in which the flow stress σ_y increases with an increase in the effective plastic strain ϵ_e^p and the effective plastic strain rate $\dot{\epsilon}_e^p$, but decreases with an increase in the non-dimensional temperature T . In Eq. (1), parameters B and n characterize the strain hardening of the material, C and $\dot{\epsilon}_0$ its strain-rate hardening, and m its thermal softening. The non-dimensional temperature T is defined as $T = (\theta - \theta_{ref}) / (\theta_m - \theta_{ref})$, where θ is the current temperature at the material point and θ_m and θ_{ref} are the presumed melting and the reference temperatures, respectively. Note that θ_m is obtained by fitting the relation (1) to the test data, and need not equal the actual melting temperature of the material. Furthermore, the hardening parameters C and n are considered to be constants, despite a known transition in strain-rate hardening in many metals between quasi-static and dynamic rates. However, this assumption's impact on the results presented here is lessened due to the exclusive consideration of high rates of deformation ($\dot{\epsilon}_e^p > 10^3/s$), which are above the transition strain rates seen in the materials of interest; e.g. see Section 4.1. The materials of the particulates and the matrix are assumed to obey the von Mises yield criterion and the associated flow rule.

Deformations of the body are governed by the balance of mass, linear momentum, moment of momentum, and internal energy, which can be found in many continuum mechanics books (e.g. see Truesdell and Noll [28], Batra [29]). Effects of heat conduction are considered with all of the plastic working converted into heating; thus the Taylor–Quinney coefficient is taken to equal 1.

We assume that the body is initially stress-free, at rest, and at a uniform temperature. It is subjected to the following boundary conditions:

$$v_2 = \begin{cases} -v_0 \hat{t} / \hat{t}_{ramp}, & 0 \leq \hat{t} \leq \hat{t}_{ramp} \\ -v_0, & \hat{t} > \hat{t}_{ramp} \end{cases} \quad \text{on } X_2 = H, \quad (2)$$

$$v_2 = 0 \quad \text{on } X_2 = 0,$$

$$T_{11} = T_{21} = Q_1 = 0 \quad \text{on } X_1 = 0 \text{ and } X_1 = H,$$

$$T_{12} = Q_2 = 0 \quad \text{on } X_2 = 0 \text{ and } X_2 = H.$$

Here, \hat{t} represents the analysis time. All bounding surfaces are taken to be thermally insulated, the top and the bottom surfaces to be smooth, and the left and the right vertical surfaces to be traction free. \mathbf{Q} equals the heat flux measured per unit area in the reference configuration, \mathbf{T} the first Piola–Kirchhoff stress tensor, and (X_1, X_2) coordinates of a point in the reference configuration with respect to rectangular Cartesian coordinate axes (e.g. see Fig. 1).

Prior to debonding, particulate/matrix interfaces are assumed to have continuous tractions, displacements, temperatures and normal components of the heat flux. Subsequent to debonding, the newly created surfaces are taken to be thermally insulated and tractions on them are computed from the cohesive relation given in Section 2.2. Since the failure occurs in less than 40 μs traction-free crack surfaces being thermally insulated is a reason-

able assumption; for longer analyses, a convective boundary condition would be necessary.

2.2. Cohesive zone relations

Fig. 2 demonstrates the traction-separation law used in the computational model. Each interface between two adjoining FEs is considered for failure, where the state variables of the two elements connected to the segment are used to compute the failure state of the segment. Fig. 2a shows one such segment, which is connected to elements 1 and 2. The outward normals to the segment surfaces are denoted by n^1 and n^2 , where the superscripts denote the connected elements. The normal tractions (σ^1, σ^2) and tangential tractions (τ^1, τ^2) on the interface are computed using each element's stress tensor σ_{ij} as shown in Eq. (3) (computations are performed for each element; superscripts are deleted for clarity); (e.g., see Truesdell and Noll [28], Batra [29]).

$$\sigma = \sigma_{ij} n_i n_j,$$

$$\tau_i = \sigma_{ij} n_j - \sigma n_i, \quad (3)$$

where a repeated index implies summation over the range ($i = 1, 2$) of the index, and σ is the Cauchy stress tensor. We denote by τ the magnitude of the tangential traction. For the segment, the normal and the tangential tractions $\hat{\sigma}$ and $\hat{\tau}$ are

$$\hat{\sigma} = (\sigma^1 + \sigma^2) / 2,$$

$$\hat{\tau} = (\tau^1 + \tau^2) / 2. \quad (4)$$

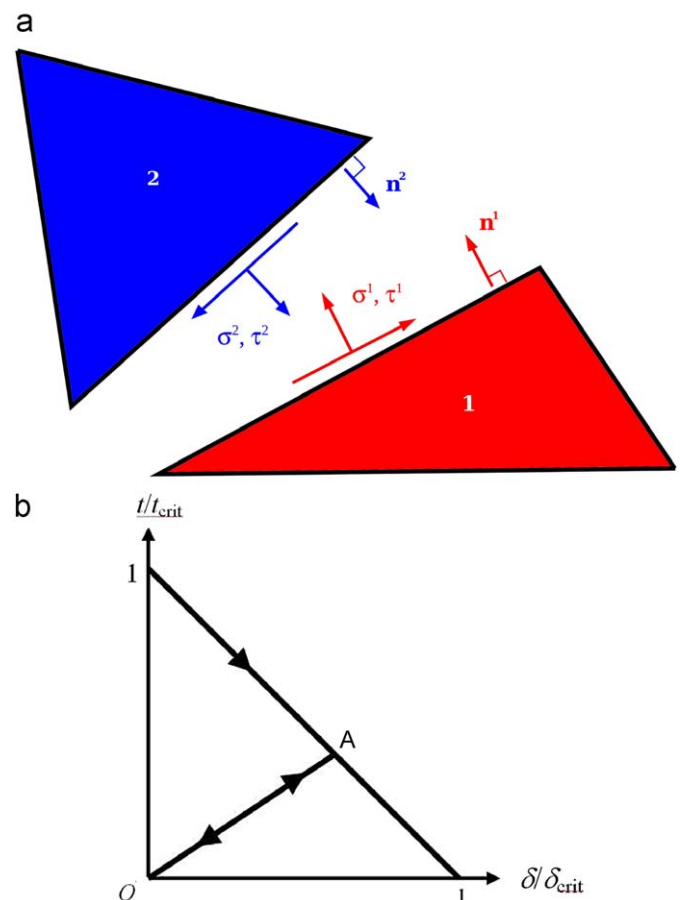


Fig. 2. Cohesive law: (a) tractions at the interface between two adjoining elements and (b) traction/opening displacement relation.

That is, $\hat{\sigma}$ and $\hat{\tau}$ equal the average of magnitudes of the normal and the tangential tractions on the two sides of the common interface; this helps reduce numerical errors introduced by the FE analysis since the magnitudes of the normal and the tangential tractions on either side of the interface are identical in a perfect continuum.

We follow Ortiz and Pandolfi [30] and define an effective traction t as:

$$t = \sqrt{\beta^{-2}|\hat{\tau}|^2 + \max(\hat{\sigma}, 0)^2}, \quad (5)$$

where $\hat{\sigma}$ and $\hat{\tau}$ are the tractions defined in Eq. (4). The parameter β determines the relative importance of the shear traction and therefore represents a form of “mode-mixity” of the crack and the material. This effective traction t is computed at every element interface at every timestep. When t reaches a critical value (defined as t_{crit}), the segment is considered failed, appropriate nodes are duplicated, a new segment is generated, and a cohesive element is introduced. The introduction of the cohesive element and the alteration of the mesh is carried out dynamically in the analysis and does not require the introduction of cohesive elements at the beginning of the analysis. The mesh alteration is also considered irreversible; that is, the material cannot “heal” and re-join two crack faces into undamaged material. The crack faces may meet and stay in contact, but they are still considered two separate segments and are dealt with by the appropriate contact algorithm to avoid inter-penetration of the material across the contact surface.

Upon failure initiation at an interface between two adjoining elements, we define an effective crack opening displacement δ (again, following Ortiz and Pandolfi [30]):

$$\delta = \sqrt{\beta^2 \delta_s^2 + \delta_n^2}, \quad (6)$$

where δ_s and δ_n are the tangential and the normal relative displacements of the two crack faces.

The cohesive zone concept indicates that the material undergoing cracking does not reach two fully traction-free surfaces until a certain amount of work has been performed (which is usually correlated to the familiar Griffith fracture energy). To accomplish this, we adopt the cohesive relation (Eq. (7)) proposed by Camacho and Ortiz [26].

$$t/t_{crit} = 1 - \delta/\delta_{crit}, \quad \dot{\delta} \geq 0;$$

$$t = \frac{t_{max}}{\delta_{max}} \delta, \quad \text{either } \dot{\delta} < 0, \text{ or } \dot{\delta} > 0 \text{ and } \delta \leq \delta_{max}$$

on the debonded interface,

$$t = 0, \quad \delta \geq \delta_{crit}. \quad (7)$$

As evident from Fig. 2b, Eq. (7) implies that the applied tractions vanish when either (a) one reaches the critical opening displacement δ_{crit} or (b) the AO segments unload as the crack closes (as indicated by the line to the origin in Fig. 2b). For $\delta \geq \delta_{crit}$ the segments are truly independent and one has a pair of traction-free thermally insulated surfaces forming the crack faces. For $\delta \leq \delta_{crit}$, a failed segment is checked for $\dot{\delta} > 0$ or $\dot{\delta} \leq 0$. In the former case, tractions are given by Eq. (7)₁ if δ is a monotonically increasing function of time for the segment; otherwise the traction is given by Eq. (7)₂ which is also used if $\dot{\delta} \leq 0$. While using Eq. (7)₂ the percentage change in both $\hat{\sigma}$ and $\hat{\tau}$ is kept the same. In Eq. (7)₂ t_{max} and δ_{max} are values of t and δ , respectively, just prior to reversing of the opening of the segment; t_{max} and δ_{max} satisfy Eq. (7)₁. It should be noted that, for monotonic increase of δ to δ_{crit} , the area, $t_{crit}\delta_{crit}/2$, under the t - δ curve is the energy per unit surface area that is dissipated during fracture and equals the Griffith fracture energy. Molinari et al. [31], among others, have

used the cohesive failure model to simulate fragmentation in a bar made of a linear elastic brittle material. They have shown that introducing a slight degree of randomness improves upto two orders of magnitude the convergence of the energy.

Determination of the appropriate critical traction t_{crit} and critical displacement δ_{crit} from experimental results obtained during dynamic loading is difficult. It has been experimentally shown (see Rosakis et al. [32]) that dynamic fracture toughness depends on crack speed. In all likelihood, the fracture toughness depends on the material, the strain-rate and temperature in the vicinity of the crack, and the initial flaw distribution.

Here, we account for temperature effects by assuming that the critical traction decreases affinely with temperature increase according to the following relation:

$$t_{crit} = t_{crit,0} \left(1 - \frac{\theta - \theta_{ref}}{\min(\theta_{melt}) - \theta_{ref}} \right), \quad (8)$$

where $t_{crit,0}$ is the critical traction at the reference temperature θ_{ref} and $\min(\theta_{melt})$ is the lower of the presumed melting temperatures of the particulate and the matrix. This assumption mimics the thermal softening in the Johnson–Cook constitutive relation (Eq. (1)); we have assumed that the critical traction decreases as the yield stress of the material decreases. The functional form (8) of the thermal softening is a postulate; experimental investigation of the dependence of fracture toughness on temperature would benefit the analysis greatly. We have tacitly assumed no strain-rate or other state-variable dependence of the critical traction $t_{crit,0}$.

The mode-mixity parameter β determines the relative strength of the material in mode-I (tensile) and mode-II (shear). Estimates for the mode mixity have been found experimentally by Chen and Ravichandran [33,34] for brittle ceramics; but little experimental work has been done for ductile metals, especially under extreme plastic deformations. Here, we have assumed that β equals 0.866, mainly for lack of information. This value of β represents a moderate mode-mixity ratio seen in a variety of ductile metals (a range between 0.7 and 0.9 has been reported for steels [32] and similar ranges have been used in simulations for brittle ceramics [26]). The effect of the value of β is assessed in Section 4.3. For mode II failure β is close to zero, t given by Eq. (5) approaches infinity and δ equals δ_n . Thus the present approach is not suitable for simulating shear dominated failure.

The critical opening displacement δ_{crit} cannot be readily determined from theoretical knowledge or experimental evidence. The pair t_{crit} and δ_{crit} define the fracture energy per unit surface area. The value of δ_{crit} affects stability of the numerical algorithm, and must be chosen such that the computations (a) are stable (which places a floor on δ_{crit}) and (b) give reasonable results for small crack openings (which places a ceiling on δ_{crit}). Here, the value of δ_{crit} has been taken to be one-tenth the mean element altitude in the specimen (which for the FE-meshes employed herein equals 0.015 mm); this value allows for stable numerical results while allowing for a fairly small crack opening displacement. With an assumed value of δ_{crit} , one can compute the value of $t_{crit,0}$ from published values of the Griffith fracture energy per unit surface area.

2.3. ASB initiation criterion

We assume that an ASB initiates at a point when the energy dissipation rate there suddenly increases by nearly an order of magnitude, the material point is deforming plastically, and deformations in its neighborhood are inhomogeneous. This differs from the ASB initiation criterion proposed by Batra and Kim [35]: an ASB initiates at a point when the shear stress there has

dropped to 80% of its peak value at that point, the material point is deforming plastically, and the deformations of the material surrounding it are highly inhomogeneous. For a simple shearing problem, Batra and Kim's criterion quantifies Marchand and Duffy's [9] experimental observation that the torque required to deform the specimen drops very rapidly when an ASB initiates. As made clear by results presented in Fig. 1 of Batra and Lear's [36] paper, the requirement of the material point deforming plastically rules out false "initiation" of an ASB due to elastic unloading. During high strain rate deformations of particulate composites, Batra and Love [18] found that this criterion can be satisfied at a material point at time \hat{t}_1 but is not necessarily satisfied at a subsequent time \hat{t}_2 due to the load exchange between particulates and the surrounding matrix.

Experimentalists generally decipher the formation of an ASB through post-mortem examination of failed specimens, calling a narrow region of intense plastic deformation a shear band. Some experimentalists have attempted to capture an ASB in situ through surface observations. As ASB formation is highly sensitive to initial defects, one must take great care when comparing either post-mortem or in situ experimental results to computational results to ensure that one is comparing the same quantity at the same material point. Furthermore, analysis of 3-dimensional deformations have shown that an ASB initiates first at a point in the interior of the body [37,38]. Thus measurements on a surface may not be true indicators of the time of initiation of an ASB.

We note that concepts of fracture toughness and/or the J-integral cannot be used to characterize the initiation and/or the propagation of an ASB; e.g. see Batra and Love [18,39]. However, these are implicitly imbedded in the cohesive zone model and are thus being tacitly used for the initiation of debonding.

Here we hypothesize that an ASB has initiated when the axial load rapidly drops.

3. Numerical solution of the problem

3.1. Brief description of the technique

We analyze the problem by the FEM, using 3-node triangular elements. The FE mesh using triangular elements provides a much larger number of potential crack paths and the mesh generation is easier than a mesh using quadrilateral elements. The problem of volumetric locking is remedied by utilizing a node-centered pressure and the finite calculus technique of Onate et al. [40].

Coupled nonlinear ordinary differential equations obtained from the weak formulation of the problem are integrated by using the conditionally stable explicit central difference method. The time step is controlled by the well documented Courant [41] condition. We employ a lumped mass matrix produced by the row-sum technique and lumped heat capacitance matrix to allow efficient solutions using the explicit central difference method. The constitutive update uses a backward Euler method similar to the radial return algorithm. Deformations during a time step are first assumed to be elastic; if they are not, the stresses, plastic strains, and temperature are updated such that the resulting state is on the yield surface. It is assumed that all plastic work results in an increase in temperature (the Taylor–Quinney coefficient is tacitly assumed to be unity). The heat conduction equation is solved and the resulting nodal temperatures are calculated by taking a forward Euler step after the mechanical step is taken; the very short time steps in this analysis allow this stepping technique to produce reasonable results.

Following the debonding/fracture process detailed in Section 2.2, the interpenetration of the material across an interface is avoided by using a contact algorithm. The algorithm checks for

interpenetration after the position/velocity update in the central difference scheme, and then interpenetrations are corrected using a symmetric sliding interface algorithm, similar to that given by Johnson and Stryk [42]. This algorithm has no "defined" master and slave surfaces, and thus is independent of the order of processing. Here, we have assumed no friction between the contacting/sliding surfaces; in reality, the friction between these surfaces is complex and difficult to model at the scale of this problem.

3.2. Verification of the computer code

The computer code has been verified by using the method of fictitious body forces, e.g. see comments following Eq. (20) of Batra and Liang [43]. In this method, a closed form expression for the solution variables is assumed, and these are substituted in the balance laws to find body forces and sources of energy needed to satisfy them. Also, initial and boundary conditions corresponding to the assumed solution are found. The initial-boundary-value problem corresponding to these initial and boundary conditions, body force and the source of internal energy is solved numerically with the code. If the computed solution agrees with the presumed analytical solution of the problem, then the code's accuracy has been verified. The results for a plane-strain shear banding problem were further compared to results from our previous code [18], and ASB initiation times were predicted to within 1% difference in heterogeneous bodies with no debonding.

4. Computation and discussion of results

We assigned the following values to material parameters for the particulates and the matrix:

Particulates (metal 1): $\rho_0 = 19,300 \text{ kg/m}^3$, $E = 400 \text{ GPa}$, $\nu = 0.29$, $\kappa = 160 \text{ W/mK}$, $c_p = 138 \text{ J/kg K}$, $\alpha = 5.3 \times 10^{-6} / \text{K}$.

$A = 730 \text{ MPa}$, $B = 562 \text{ MPa}$, $C = 0.029$, $m = 1.0$, $n = 0.0751$, $\theta_m = 1700 \text{ K}$, $\dot{\epsilon}_0 = 1 \times 10^{-6} / \text{s}$.

Matrix (metal 2): $\rho_0 = 9200 \text{ kg/m}^3$, $E = 255 \text{ GPa}$, $\nu = 0.29$, $\kappa = 100 \text{ W/mK}$, $c_p = 382 \text{ J/kg K}$, $\alpha = 15.0 \times 10^{-6} / \text{K}$.

$A = 150 \text{ MPa}$, $B = 546 \text{ MPa}$, $C = 0.0838$, $m = 1.0$, $n = 0.208$, $\theta_m = 1225 \text{ K}$, $\dot{\epsilon}_0 = 1 \times 10^{-6} / \text{s}$.

Here ρ_0 is the initial mass density, E the Young's modulus, ν the Poisson's ratio, c_p the specific heat, κ the thermal conductivity, and α the coefficient of thermal expansion. The reference temperature θ_{ref} was taken to be 293 K.

The parameters for the cohesive law were taken to be:

Metal 1–metal 1: $t_{crit,0} = 1.8 \text{ GPa}$, $\delta_{crit} = 1.5 \times 10^{-2} \text{ mm}$, $\beta = 0.866$.

Metal 2–metal 2: $t_{crit,0} = 1.5 \text{ GPa}$, $\delta_{crit} = 1.5 \times 10^{-2} \text{ mm}$, $\beta = 0.866$.

Metal 1–metal 2: $t_{crit,0} = 0.8, 1.0, 1.2, 1.5 \text{ GPa}$, $\delta_{crit} = 1.5 \times 10^{-2} \text{ mm}$, $\beta = 0.866$.

These values are computed from fracture energies for the respective materials, realizing that the area under the curve in Fig. 2b equals the fracture energy per unit surface area. For $t_{crit,0} = 1.8 \text{ GPa}$, $\delta_{crit} = 0.015 \text{ mm}$, energy dissipated per unit surface area during monotonic debonding equals $13,500 \text{ J/m}^2$. Effects of varying strength $t_{crit,0}$ of the particulate/matrix interface and β on the ASB formation have been studied.

Square specimens of various sizes (1, 2 and 4 mm side) were given random distributions of particulates with radius ranging from 50 to 80 μm , holding the volume fraction of particulates to $31 \pm 0.2\%$. The specimens were meshed with triangular elements with an approximate side length of 0.02 mm. The particulates were arranged such that there was a minimum of three triangular elements (0.06 mm) between any two particulates. Subsequent to

the initial rise in the applied axial velocity, each specimen was subjected to plane strain compression at a nominal axial strain rate of 10,000/s.

4.1. Results without debonding

As a reference, each specimen was deformed without allowing debonding and fracture to occur. ASBs formed in a way consistent with that given in Batra and Love [18]; i.e. large plastic strains and a nearly discontinuous velocity field at about 45° to the loading axis. Figs. 3a and b exhibits contours of the effective plastic strain and the vertical velocity component for one of these cases. It is clear that one dominant ASB with effective plastic strain of ~ 1 and inclined at ~ 45° to the loading direction formed. Once the ASB had formed the specimen was divided into two regions; the lower virtually stationary pyramid, and the upper one moving downwards with the velocity imposed on the top surface. There is a sharp gradient in the velocity field between these two regions where strain rates and the effective plastic strain are quite large.

Fig. 4 exhibits fringe plots of the velocity field at $t = 25 \mu s$ and time histories of the effective plastic strain rate at four points. Points 1 and 3 are within the ASB, and 2 and 4 are outside the ASB; points 1 and 2 are in the matrix, and points 3 and 4 in the particulates. It is clear that the effective plastic strain at these four points are more than $10^4/s$ except at late times when the ASB has developed. The strain rates at points 1 and 3 increase by a factor of 10 as the ASB develops. It is clear from these results that the error, if any, in not considering the dependence of C in Eq. (1) upon the strain rate is negligible.

We note that the random distribution of the particulates does not significantly impact the ASB initiation time. Fig. 5 shows the axial load versus the nominal axial compressive strain for six microstructures with approximately 31% volume fraction of particulates. The axial load is computed from tractions at nodes on the top surface where axial velocity is prescribed, and taking the specimen dimension in the X_3 -direction equal to 1 mm. Note that the sudden drop in the applied load (indicative of shear band formation) occurs at the axial strain between 30% and 34% for each of the specimens. Thus the difference between the minimum and the maximum ASB time is 12%.

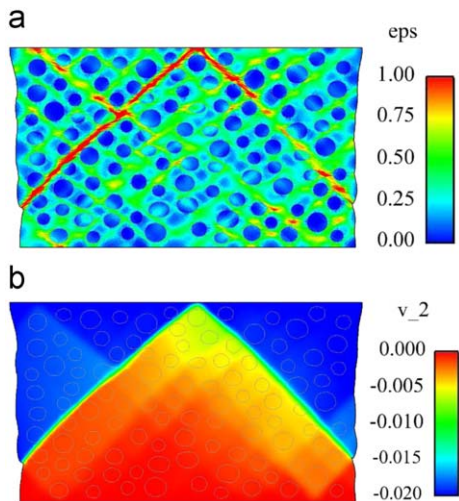


Fig. 3. Contours of (a) effective plastic strain and (b) vertical velocity at time $t = 23.8 \mu s$ for a particulate composite subjected to plane strain compression at a nominal axial strain rate of 10,000/s.

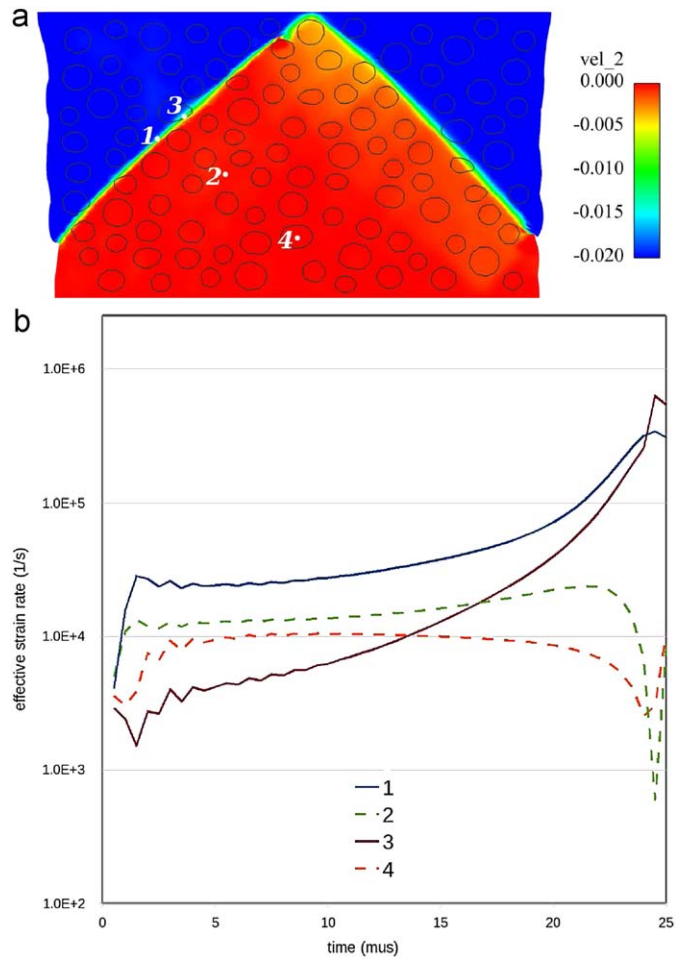


Fig. 4. Strain rate histories for four points; position of points at $t = 25 \mu s$ shown in (a).

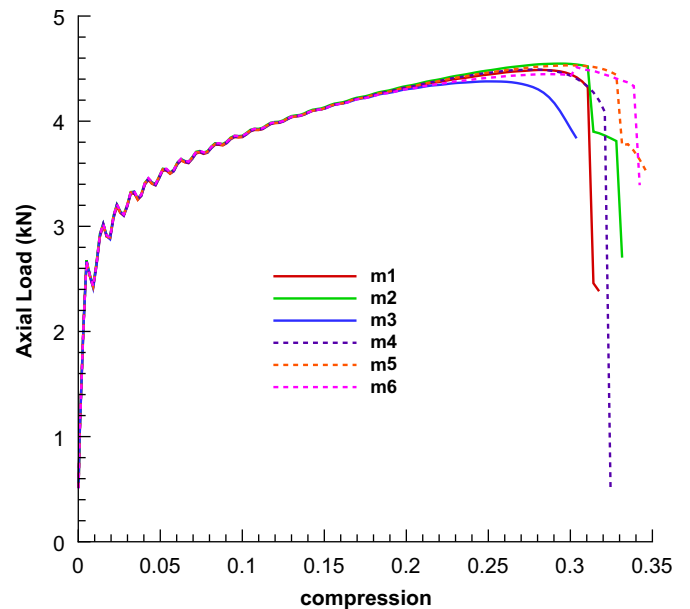


Fig. 5. Axial load versus axial compressive strain curves for six random microstructures of 31% volume fraction particulate.

4.2. Results with material failure

4.2.1. Effect of specimen size

When simulating microstructures, the question of an appropriate size for the specimen always arises. To examine this effect, we subjected $1\text{ mm} \times 1\text{ mm}$, $2\text{ mm} \times 2\text{ mm}$, and $3\text{ mm} \times 3\text{ mm}$ specimens to plane strain compression. The particulates were randomly generated with diameters ranging from 100 to $160\ \mu\text{m}$, and their volume fractions equaled $31\% \pm 0.2\%$. The finite element size was held constant throughout all of the simulations. The critical traction $t_{crit,0}$ on the particulate/matrix interface was taken to be 1.0 GPa , and material properties were assumed not to depend on the particulate diameter.

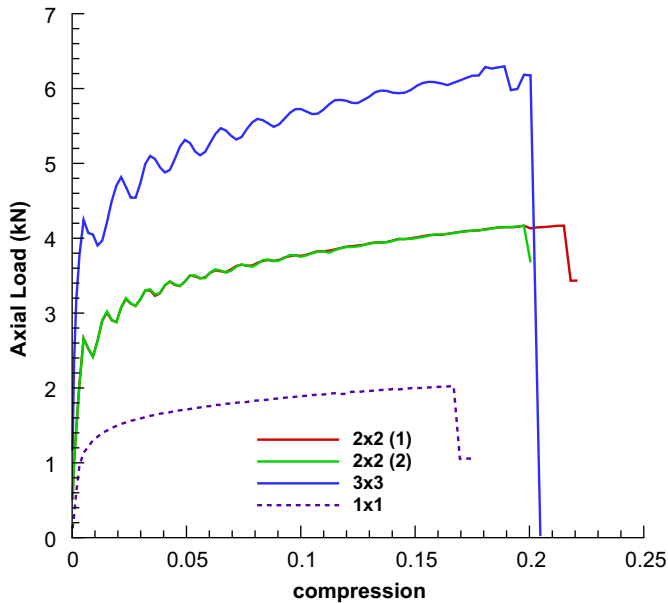


Fig. 6. Axial load versus axial compressive strain curves for three different specimen sizes (mm \times mm).

Fig. 6 shows the load versus compression curves for all three specimen sizes. Note there are two $2\text{ mm} \times 2\text{ mm}$ specimens; these two curves show the typical variation caused by slightly different particulate arrangements but the same volume fraction; this is similar to the effect of microstructures studied in Section 4.1. Note that the ASB initiation time for the $3\text{ mm} \times 3\text{ mm}$ case coincides with that of one of the $2\text{ mm} \times 2\text{ mm}$ specimens, but the $1\text{ mm} \times 1\text{ mm}$ specimen shows a substantially earlier load drop. This difference can possibly be attributed to the number of particulates in the specimen; in the $1\text{ mm} \times 1\text{ mm}$ specimen, the small number of particulates allows an ASB to form entirely in the matrix at a substantially earlier time. With a sufficient number of particulates, the formation of the ASB is impeded by the harder particulates; this effect was also seen in Batra and Love [18]. Note that the oscillations seen in the load/compression curves are due to the stress-wave reflections in the specimen. The period of these reflections is related to the size of the specimen and thus, a $3\text{ mm} \times 3\text{ mm}$ specimen is the largest plausible at this loading rate without the stress wave effects becoming significant. The difference in the acoustic impedances of the particulate and the matrix materials affects reflections, refractions and the transmission of waves at interfaces; the acoustic impedance of metal 1 equals 1.81 times that of metal 2. The time integration scheme should be checked for not producing excessive oscillations in the solution due to the acoustic impedance mismatch between the particulate and the matrix.

Until the axial compressive strain of 0.15, the axial compressive load essentially scales with the specimen width, i.e., the axial force for the 3×3 specimen is three times that for the 1×1 specimen.

For further analyses, we use the $2\text{ mm} \times 2\text{ mm}$ specimen, as it gives reasonable results with substantially less computational effort than the $3\text{ mm} \times 3\text{ mm}$ specimen.

4.2.2. Crack-tip pinning

One potential problem that arose early in the analyses is that of crack-tip “pinning” (see Fig. 7) which led to a collapse of an element and the termination of the analysis. This phenomenon

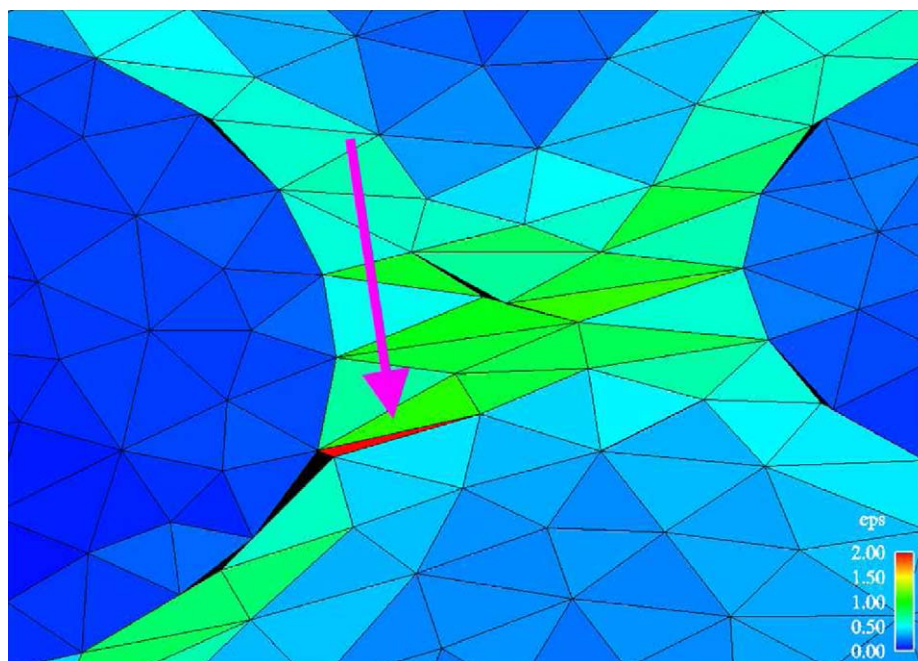


Fig. 7. Crack “pinning” phenomenon that can result in termination of the analysis.

occurs due to compressive stress fields in the domain, which are typical of this loading scenario. A crack nucleates due to shear stress at 45° to the loading direction on the particulate/matrix interface and propagates until it is arrested due to this compressive field. Subsequently, the compressive deformations tend to crush the element near the crack tip in the softer matrix. To allow the analysis to proceed, we resorted to element deletion

when the minimum altitude of an element became 1/10,000th of its original value. The element was simply removed from computation (thus removing a small amount of mass from the problem and creating a small void) and contact surfaces were updated and the analysis continued. For the problems studied herein at most ten out of several thousand elements were deleted; thus the error caused due to the deletion of these elements is negligible.

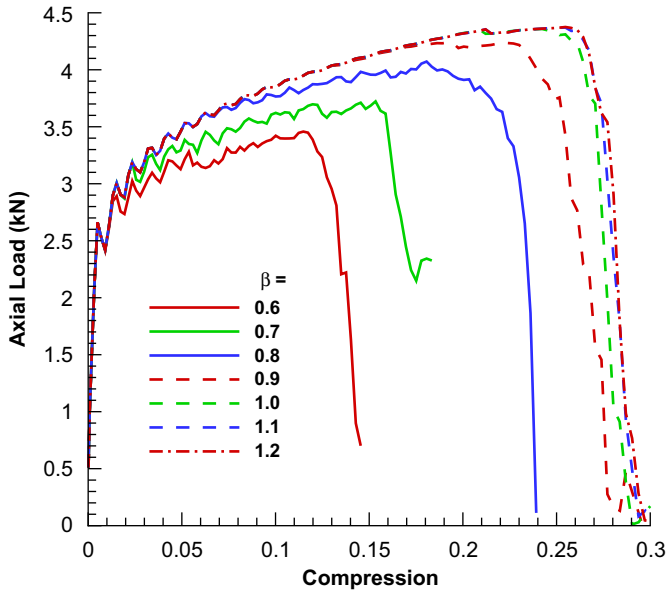


Fig. 8. Axial load versus axial compressive strain curves for various values of the mode-mixity parameter β .

4.3. Effect of mode mixity

The parameter β in the cohesive law (see Eqs. (5) and (6)) determines the critical traction under mixed-mode (normal and shear) loading conditions. One determines $t_{crit,0}$ from the pure mode I fracture toughness, and then computes β using the pure mode II fracture toughness. The cohesive law then determines the critical traction under combined loading. Unfortunately, experimental determination of mode II fracture toughness is difficult, particularly under dynamic loading. While there are reasonable estimates for β for monolithic materials (see Chen and Ravichandran [33,34]; Pandolfi et al. [32]), the strength of the interface due to shear is much less well characterized.

Fig. 8 shows the load versus compression for a single microstructure with a range of values of β for the interface. The critical traction was taken to be $t_{crit} = 1.2$ GPa. We consider values of β ranging from 0.6 to 1.2, which should contain the physically meaningful solutions to the problem (note that functions in Eqs. (5) and (6) become singular as β tends to zero or infinity). The load versus compression curves are quite different over this range of β , although the load versus compression curves seem to “converge” for $\beta \geq 1.0$. Further evidence of this is seen in Fig. 9; note the similarity of the results for $\beta = 1.0$ and 1.2.

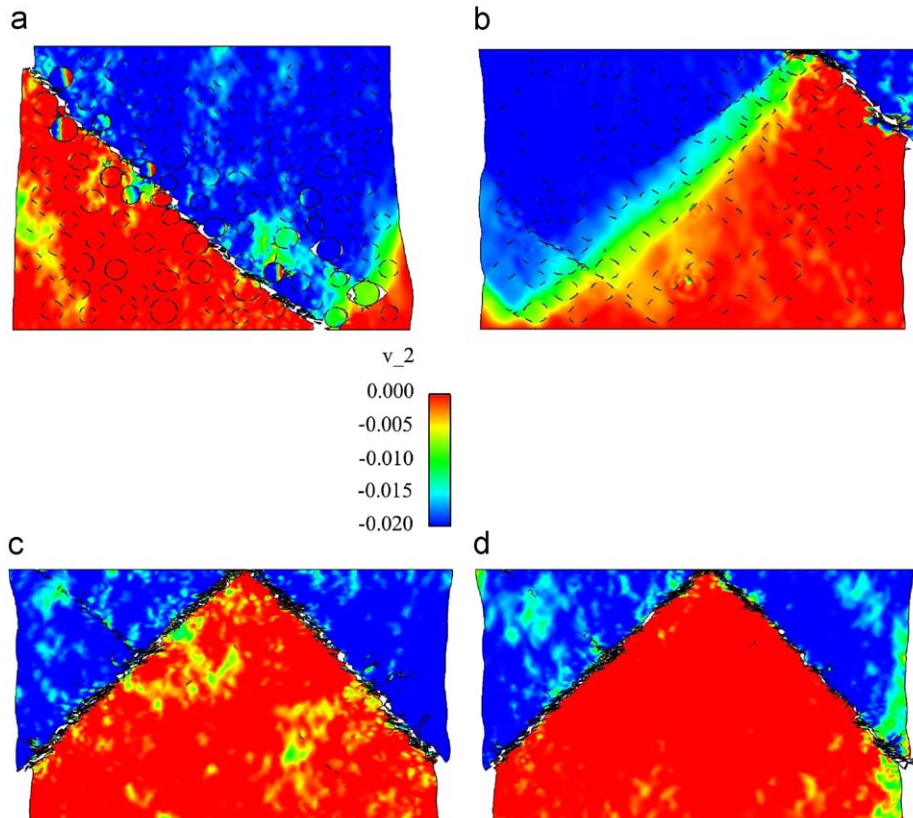


Fig. 9. Contours of vertical velocity for a single specimen for mode-mixity parameter and times of (a) $\beta = 0.6$ and $\hat{t} = 13.2 \mu\text{s}$, (b) $\beta = 0.8$ and $\hat{t} = 19.4 \mu\text{s}$, (c) $\beta = 1.0$ and $\hat{t} = 22.8 \mu\text{s}$, and (d) $\beta = 1.2$ and $\hat{t} = 22.8 \mu\text{s}$. Dark lines denote cracks/new interfaces.

The dark circles in Fig. 9 imply that the matrix has debonded from the particulate. Also white regions imply voids or cracks. The deformed shapes and locations of ASBs for $\beta = 0.6$ and 0.8 are quite different from those for $\beta = 1.0$ and 1.2 . Thus the mode-mixity or the cohesive failure criterion plays dominant roles in not only the time of formation of an ASB but also in their spatial locations. A smaller value of β makes the interface more susceptible to shear fracture; for $\beta = 0.6$, many of the particulate matrix interfaces are fractured prior to the development of the ASB. As one would expect this debonding of particulates and matrix materials leads to distinctly different local stress states and velocity fields which in turn change the ASB evolution as evinced by differences in results shown in Figs. 9a and 9b. The ASB initiation time for $\beta = 0.6$ is nearly one-half of that for $\beta = 1.1$. Without experimental data for mixed-mode loading for particulate/matrix interfaces, we continue to use $\beta = 0.866$ for the interface as well as for the monolithic materials.

4.4. Effect of interfacial strength

We note that experimental data on the particulate/matrix interfacial strength is not readily available in the open literature. Accordingly, we conduct a parametric study and consider three values of this strength, namely $t_{crit,0} = 1.0, 1.2,$ and 1.5 GPa; results for the no debonding case are also presented.

The results for a single microstructure for all three values of the critical traction $t_{crit,0}$ and for the no debonding case are shown in Fig. 10, and the plot of axial load versus axial compressive strain for these four cases is exhibited in Fig. 11. Note that reducing the interface strength generally decreased the ASB

initiation time. Furthermore, the lower two values of the interface strength exhibited significant “debonding” of the particulates from the matrix prior to localization, which is evinced from the load versus compression curve deviating from the “no fracture” case. The 1.2 and 1.5 GPa critical stresses

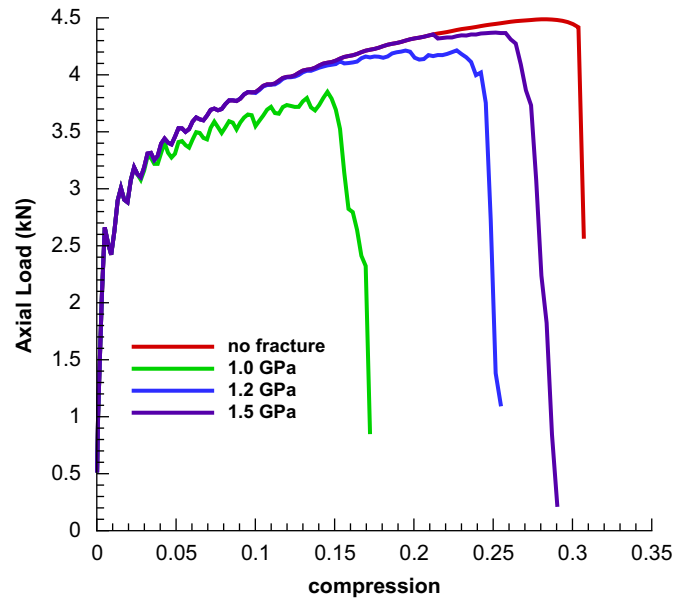


Fig. 11. Axial load versus axial compressive strain for three values of the critical traction and the no fracture case for a single specimen.

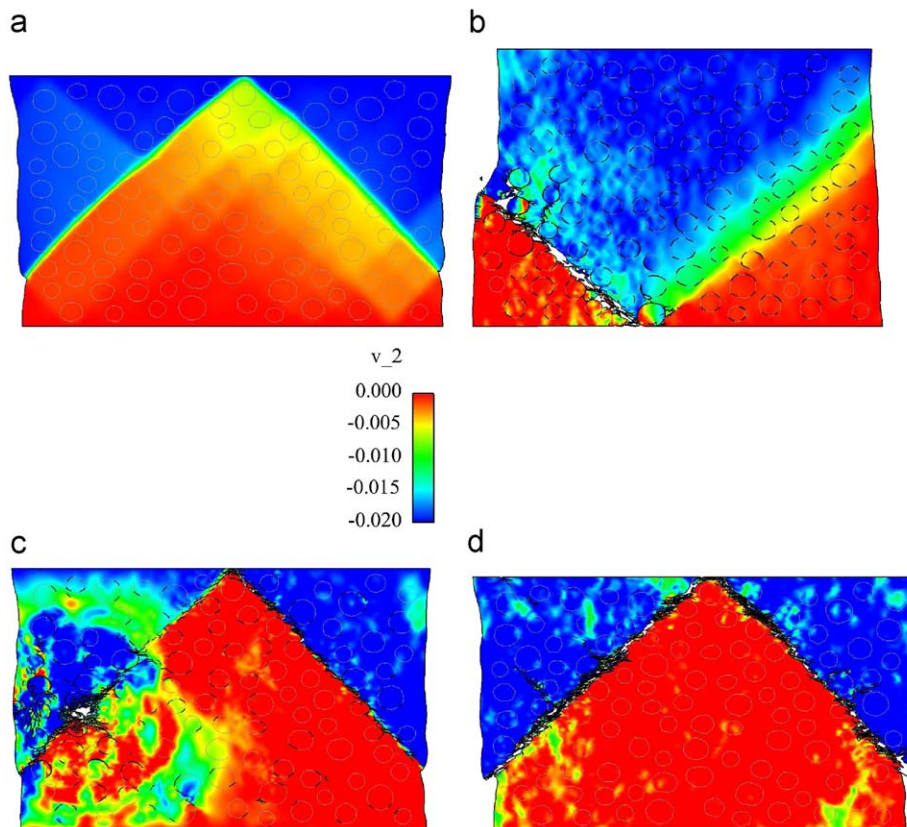


Fig. 10. Contours of vertical velocity for a single specimen for critical tractions and times of (a) no fracture and $\hat{t} = 23.8 \mu\text{s}$, (b) $t_{crit,0} = 1.0$ GPa and $\hat{t} = 15.0 \mu\text{s}$, (c) $t_{crit,0} = 1.2$ GPa and $\hat{t} = 20.4 \mu\text{s}$, and (d) $t_{crit,0} = 1.5$ GPa and $\hat{t} = 23.0 \mu\text{s}$. Dark lines denote cracks/new interfaces while light gray lines denote particulate/matrix interfaces that are still bonded.

showed fracture almost exclusively along the ASB through the bulk material (mainly in the matrix) at fairly late times; note the agreement with the “no fracture” case in the load/compression curve to 20% compression.

Examining the dissipation rate to observe the initiation of an ASB reveals some interesting results. For the case of no fracture, Fig. 12a shows the expected dramatic rise in the dissipation rate for an element in the ASB. For a relatively high value of the critical traction, $t_{crit,0} = 1.5$ GPa in Fig. 12c, the dissipation rates show a similar trend. However, for a relatively low value of the critical traction ($t_{crit,0} = 1.0$ GPa in Fig. 12b), the dissipation rate increases but there is no dramatic change of slope (other than the brief

spikes at the time of fracture of segments near the element in question), despite the dramatic drop in load shown in Fig. 11. Examining the details of deformations reveals the difference between these two cases. In the $t_{crit,0} = 1.0$ GPa case, fracture occurs while the axial compressive load is increasing, with little plastic strain near the fractured surfaces (thus indicating “brittle” fracture). The ASB forms along a path through the matrix connecting multiple sites of brittle fractures, and the load drop is due to a combination of the decrease in strength of the material induced by fracture surfaces and the thermal softening of the material in the ASB. For the higher value of the critical traction $t_{crit,0} = 1.5$ GPa, an ASB forms just as in the case of no fracture, and the load drop occurs due to the thermal softening of the material along the ASB. A crack develops in the shear banded material. The crack and the ASB include many particulate/matrix interfaces. The rapid increase in the energy dissipation rate is not a good indicator of ASB formation in the presence of weak particulate/matrix interfaces.

5. Remarks

Batra and Love [39] used the nodal release technique to simulate crack propagation in mode I and mode II deformations of a functionally graded thermoviscoplastic body deformed at high strain rates. When a prespecified local failure criterion was met at a node, it was split into two nodes an infinitesimal distance apart and the nodal connectivity was modified. The brittle failure was assumed to ensue at a point when the maximum principal stress there exceeds three times the quasi-static yield stress, and the ductile failure was initiated when the effective plastic strain equals 1.5. They thus studied crack initiation and propagation in plane strain deformations of an inhomogeneous plate deformed in either tension or shear. Batra and Lear [36] had employed a similar procedure to study crack initiation and propagation in a prenotched steel plate impacted on the notched side, and found computed results to be in reasonable qualitative agreement with those observed experimentally. Hassan and Batra [44] used a similar procedure to study delamination between adjoining layers in a laminated composite plate.

Both the cohesive zone technique and the nodal release method assume that fracture initiates instantaneously once the respective failure criterion has been satisfied at a point. Whereas in the cohesive zone procedure the rate of decrease to zero of surface tractions depends on the rate of increase of the crack opening displacement δ , in the nodal release technique it is decided empirically. In both methods surface tractions are decreased gradually to keep the numerical algorithm stable and mitigate effects of shock waves being released from the crack faces. The mode-mixity of deformations near a crack-tip is approximately accounted for in the cohesive zone failure equations (5) and (6) through the parameter β , it is not considered in the nodal release technique employed in [39,36]. Note that β cannot be assigned either an extremely large or a very small value; otherwise the computational algorithm becomes unstable.

The postulate that the critical traction drops with temperature (see Eq. (8)) was chosen because it allows for fracture in the high temperature regions produced by ASBs. This assumption, however, is not unique—analyses that utilized a critical strain to failure were conducted and the results were qualitatively similar to those given by the temperature dependent traction. In reality, the cohesive zone relation should depend on several state variables, particularly the strain rate and the temperature. This dependence is still an open area of research and published data on it is not available in the open literature.

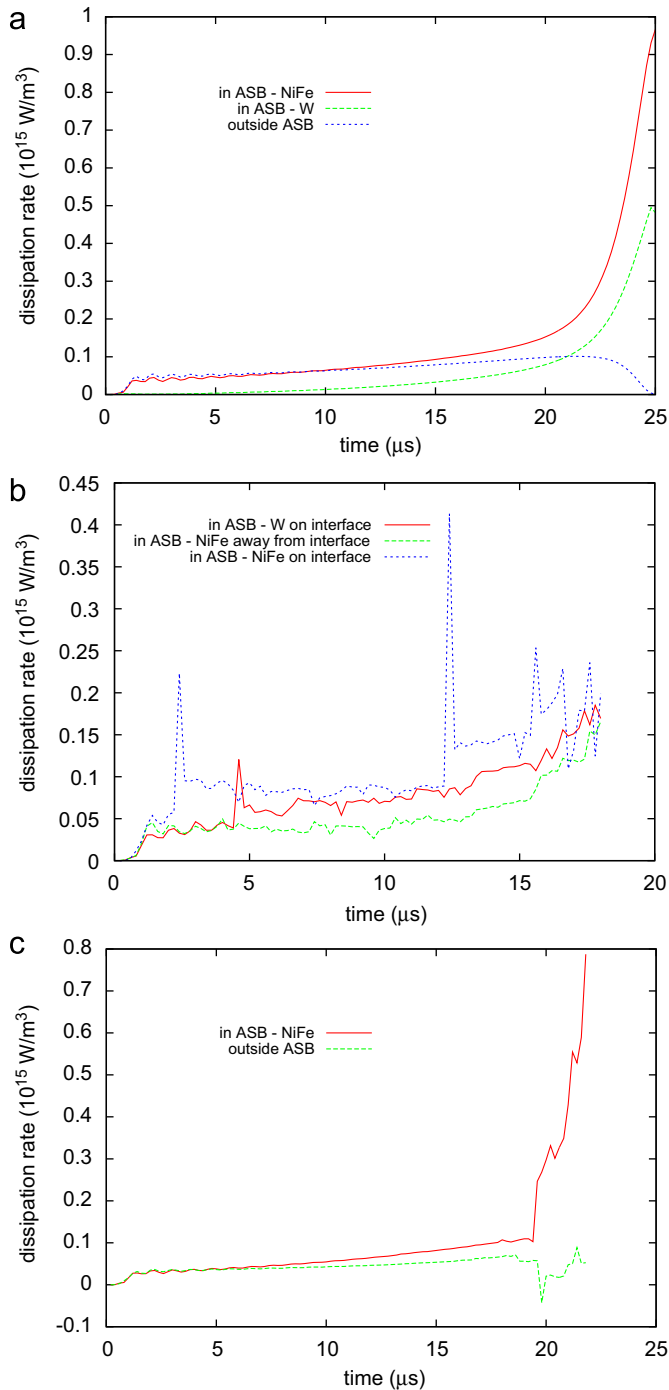


Fig. 12. Energy dissipation rate versus time for points in the body with (a) no fracture, (b) $t_{crit,0} = 1.0$ GPa, and (c) $t_{crit,0} = 1.5$ GPa.

Here we have employed the Johnson–Cook relation to model the thermo-visco-elasto-plastic response of the particulate and the matrix. It is shown in [45,46] that even when different constitutive relations have been calibrated to give identical shear stress versus shear strain curve at one nominal strain rate, they do not predict the same ASB initiation time and the post-localization response.

6. Conclusions

We have studied the plane strain transient thermomechanical deformations of a particulate composite with the finite element method. Various representative volume elements comprised of approximately 31% metallic particulates dispersed in a metallic matrix were subjected to plane strain compression at an axial nominal strain rate of 10,000/s. Effects of heat conduction, strain and strain-rate hardening, thermal softening, and debonding at interfaces and fracture in each material have been incorporated in the analysis. Computed results for various values of the interface strength parameter have indicated that the interface strength noticeably influences the shear band susceptibility and the load carrying capacity of the composite. Furthermore, debonding between the particulates and the matrix does not deter the formation and the propagation of adiabatic shear bands.

The present work suggests that additional studies are needed to find reasonable values for the critical traction t_{crit} and the mode-mixity parameter β in the cohesive zone relation. Furthermore, the cohesive zone relation should also take into account the strains, strain-rates, and temperatures experienced by the body; here we have used a t_{crit} that is invariant with respect to strain and strain-rate and has a presumed affine softening due to temperature. Experimental investigation into the strength of these interfaces in both mode I and mode II would allow this type of analysis to give results that compare well with experimental findings and then could be used to help predict the onset of adiabatic shear bands in particulate composites, and appropriately design interfaces and composites. The present work suggests that strong interfaces delay the adiabatic shear band initiation.

Acknowledgments

BML's work was supported by the Weapons and Materials Research Directorate, US Army Research Laboratory, and RCB's work was partially supported by the Office of Naval Research grant N00014-06-1-0576 to Virginia Polytechnic Institute and State University with Dr. Y.D.S. Rajapakse as the program manager, RCB's work was also sponsored by the Army Research Laboratory and was accomplished under Cooperative Agreement Number W911NF-06-2-0014. The views and conclusions contained in this document are those of the authors and should not be interpreted as representing the official policies, either expressed or implied, of the Army Research Laboratory or the US Government. The US Government is authorized to reproduce and distribute reprints for Government purposes notwithstanding any copyright notation hereon. Computational resources were provided by the Army High Performance Computing Center.

References

- [1] Magness L, Farrand T. Deformation behavior and its relationship to the penetration performance of high-density KE penetrator materials. In: Proceedings of the 1990 army science conference, West Point, NY, 1990.
- [2] Tresca H. On further application to the flow of solids. Proc Inst Mech Eng 1878;30:301–45.
- [3] Massey H. The flow of metal during forging. Proc Manchester Assoc Eng 1928;21–6.
- [4] Zener C, Holloman J. Effect of strain rate upon plastic flow. J Appl Phys 1944;15:22–32.
- [5] Clifton R. Adiabatic shear banding. In: Material response to ultra-high loading rates, Washington, DC, NMAB-365, 1980.
- [6] Bai Y. Thermoplastic instability in simple shear. J Mech Phys Solids 1982;30:195–207.
- [7] Wright T, Walter J. On stress collapse in adiabatic shear bands. J Mech Phys Solids 1987;85:701–20.
- [8] Wright T, Batra R. The initiation and growth of adiabatic shear bands. Int J Plasticity 1985;1:205–12.
- [9] Marchand A, Duffy J. An experimental study of the formation process of adiabatic shear bands in a structural steel. J Mech Phys Solids 1988;36:251–83.
- [10] Batra R. Effect of material parameters on the initiation and growth of adiabatic shear bands. Int J Solids Struct 1987;23:1435–46.
- [11] Bai Y, Dodd B. Adiabatic shear localization: occurrence, theories, and applications. Oxford: Pergamon Press; 1992.
- [12] Perzyna P, editor. Localization and fracture phenomenon in inelastic solids. Berlin: Springer; 1998.
- [13] Tomita Y. Simulation of plastic instabilities in solid mechanics. Appl Mech Rev 1994;47:171–205.
- [14] Wright T. The physics and mathematics of adiabatic shear bands. Cambridge: Cambridge University Press; 2002.
- [15] Zhou M, Needleman A, Clifton R. Finite-element simulation of shear localization in plate impact. J Mech Phys Solids 1994;42:423–58.
- [16] Zhou M. The growth of shear bands in composite microstructures. Int J Plasticity 1998;14:733–54.
- [17] Batra R, Wilson N. Adiabatic shear bands in plane strain deformations of a wha. Int J Plasticity 1998;14:43–60.
- [18] Batra R, Love B. Mesoscale analysis of shear bands in high strain rate deformations of tungsten/nickel–iron composites. J Thermal Stresses 2005;28:747–82.
- [19] Batra R, Love B. Consideration of microstructural effects in the analysis of adiabatic shear bands in a tungsten heavy alloy. Int J Plasticity 2006;22:1858–78.
- [20] Charalambakis N, Baxevis T. Adiabatic shearing of non-homogenous thermoviscoplastic materials. Int J Plasticity 2004;20:899–914.
- [21] Zhu Z, Batra R. Analysis of shear banding in plane strain compression of a bimetallic thermally softening viscoplastic body containing an elliptical void. J Eng Mater Technol 1991;113:382–95.
- [22] Batra R, Kwon Y. Adiabatic shear banding in a bimetallic body. Acta Mech 1989;77:281–97.
- [23] Dugdale D. Yielding of steel sheets containing slits. J Mech Phys Solids 1960;8:100–4.
- [24] Barenblatt G. The mathematical theory of equilibrium of cracks in brittle fracture. Adv Appl Mech 1962;7:55–129.
- [25] Xu X-P, Needleman A. Numerical simulations of fast crack growth in brittle solids. J Mech Phys Solids 1994;42:1397–434.
- [26] Camacho G, Ortiz M. Computational modeling of impact damage in brittle materials. Int J Solids Structures 1996;33:2899–938.
- [27] Johnson G, Cook W. A constitutive model for metals subjected to large strains, high strain-rates, and high temperatures. In: Proceedings of the seventh international symposium on ballistics, 1983. p. 541–7.
- [28] Truesdell C, Noll W. The nonlinear field theories of mechanics. Berlin: Springer; 1965.
- [29] Batra R. Elements of continuum mechanics. Reston, VA: American Institute of Aeronautics and Astronomy; 2005.
- [30] Ortiz M, Pandolfi A. Finite-deformation irreversible cohesive elements for three-dimensional crack-propagation analysis. Int J Numer Meth Eng 1999;44:1267–82.
- [31] Molinari J, Gazonas G, Raghupathy R, Rusinek A, Zhou F. The cohesive element approach to dynamic fragmentation: the question of energy convergence. Int J Numer Meth Eng 2007;69:484–503.
- [32] Pandolfi A, Guduru P, Ortiz M, Rosakis A. Three dimensional cohesive-element analysis and experiments of dynamic fracture in c300 steel. Int J Solids Struct 2000;37:3733–60.
- [33] Chen W, Ravichandran G. Dynamic compressive behavior of ceramics under lateral confinement. J Phys IV 1994;4:177–82.
- [34] Chen W, Ravichandran G. Static and dynamic compressive behavior of aluminum nitride under moderate confinement. J Am Ceramic Soc 1996;79:579–84.
- [35] Batra R, Kim C. Analysis of shear banding in twelve materials. Int J Plasticity 1992;8:425–52.
- [36] Batra R, Lear M. Adiabatic shear banding in plane strain tensile deformations of eleven thermoelastoviscoplastic materials with finite thermal wave speed. Int J Plasticity 2005;21:1521–45.
- [37] Batra R, Ravisankar M. Three-dimensional numerical simulation of the Kalthoff experiment. Int J Fracture 2000;105:161–86.
- [38] Batra R, Romano R. Failure of dynamically loaded thermoelastoviscoplastic rectangular plate. AIAA J 2007;45:2015–23.
- [39] Batra R, Love B. Crack propagation due to brittle and ductile failures in microporous thermoelastoviscoplastic functionally graded materials. Eng Fracture Mech 2005;72:1954–79.

- [40] Onate E, Rojek J, Taylor R, Zienkiewicz O. Non-linear dynamic analysis of solids using linear triangles and tetrahedra. In: Onate E, Owen D, editors. Proceedings of the VII international conference on computational plasticity, Barcelona, 2003.
- [41] Courant R, Friedrichs K, Lewy H. Über die partiellen differenzengleichungen der mathematischen physik. *Mathematische Annalen* 1928;100:32–74.
- [42] Johnson G, Stryk R. Symmetric contact and sliding interface algorithms for intense impulsive loading computations. *Comp Meth Appl Mech Eng* 2001;190:4531–49.
- [43] Batra R, Liang X. Finite deformations of smart structures. *Comp Mech* 1997;20:427–38.
- [44] Hassan N, Batra R. Modeling damage in polymeric composites. *Composites B* 2008;39:66–82.
- [45] Batra R, Kim C. Effect of viscoplastic flow rules on the initiation and growth of shear bands at high strain rates. *J Mech Phys Solids* 1990;38:859–74.
- [46] Batra R, Chen L. Effect of viscoplastic relations on the instability strain, shear band initiation strain, the strain corresponding to the minimum shear band spacing, and the band width in a thermoviscoplastic materials. *Int J Plasticity* 2001;17:1465–89.